JGR Atmospheres

RESEARCH ARTICLE
10.1029/2020JD033682

Climatology and Evolution of the Antarctic Peninsula Föhn Wind-Induced Melt Regime From 1979–2018

M. K. Laffin[1], C. S. Zender[1,2], S. Singh[2], J. M. Van Wessem[3], C. J. P. P. Smeets[3], and C. H. Reijmer[3]

[1]Department of Earth System Science, University of California, Irvine, CA, USA, [2]Department of Computer Science, University of California, Irvine, CA, USA, [3]Institute for Marine and Atmospheric Research Utrecht, Utrecht University, Utrecht, Netherlands

Key Points:

- We use machine learning, trained with surface observations to identify föhn winds on the Antarctic Peninsula and their impact on melt
- Föhn-induced melt trends mirror surface temperature trends with increased melt from 1979 to 1998 and stable/decreased melt from 1999 to 2018
- Föhn occurrence, or the number of hours föhn melt occurs, drives annual föhn-induced melt variability and evolution

Correspondence to:
M. K. Laffin,
mlaffin@uci.edu

Citation:
Laffin, M. K., Zender, C. S., Singh, S., Van Wessem, J. M., Smeets, C. J. P. P., & Reijmer, C. H. (2021). Climatology and evolution of the Antarctic Peninsula föhn wind–induced melt regime from 1979–2018. *Journal of Geophysical Research: Atmospheres*, *126*, e2020JD033682. https://doi.org/10.1029/2020JD033682

Received 10 AUG 2020
Accepted 6 JAN 2021

Author Contributions:

Conceptualization: M. K. Laffin, C. S. Zender, S. Singh
Data curation: J. M. Van Wessem, C. J. P. P. Smeets, C. H. Reijmer
Formal analysis: M. K. Laffin
Funding acquisition: M. K. Laffin, C. S. Zender, S. Singh
Investigation: M. K. Laffin
Methodology: M. K. Laffin, C. S. Zender, S. Singh
Resources: C. S. Zender, J. M. Van Wessem
Software: M. K. Laffin, S. Singh
Supervision: C. S. Zender, S. Singh
Validation: M. K. Laffin, C. S. Zender
Writing – original draft: M. K. Laffin
Writing – review & editing: M. K. Laffin, C. S. Zender, S. Singh, J. M. Van Wessem, C. J. P. P. Smeets, C. H. Reijmer

Abstract Warm and dry föhn winds on the Antarctic Peninsula (AP) cause surface melt that can destabilize vulnerable ice shelves. Topographic funneling of these downslope winds through mountain passes and canyons can produce localized wind-induced melt that is difficult to quantify without direct measurements. Our Föhn Detection Algorithm (FöhnDA) identifies the surface föhn signature that causes melt from measurement by 12 Automatic Weather Stations on the AP, that train a machine learning model to detect föhn in 5 km Regional Atmospheric Climate Model 2 (RACMO2.3p2) simulations and in the ERA5 reanalysis model. We estimate the fraction of AP surface melt attributed to föhn and possibly katabatic winds and identify the drivers of melt, temporal variability, and long-term trends and evolution from 1979–2018. We find that föhn wind-induced melt accounts for 3.1% of the total melt on the AP and can be as high at 18% close to the mountains where the winds funnel through mountain canyons. Föhn-induced surface melt does not significantly increase from 1979–2018, despite a warmer atmosphere and more positive Southern Annular Mode. However, a significant increase (+0.1 Gt y-1) and subsequent decrease/stabilization occur in 1979–1998 and 1999–2018, consistent with the AP warming and cooling trends during the same time periods. Föhn occurrence, more than föhn strength, drives the annual variability in föhn-induced melt. Long-term föhn-induced melt trends and evolution are attributable to seasonal changes in föhn occurrence, with increased occurrence in summer, and decreased occurrence in fall, winter, and early spring over the past 20 years.

Plain Language Summary Surface melt on the glaciers and floating ice shelves of the Antarctic Peninsula can contribute to sea-level rise via run-off to the ocean and by ice-shelf destabilization and reduced buttressing against glacier flow to the ocean. Surface melt on the Antarctic Peninsula has traditionally been attributed to sunlight melting snow although more recent studies demonstrate significant contributions in all seasons from warm, downslope winds called föhn winds. It is important to understand where these winds cause melt, when they cause melt, how much melt, and are they changing through time? We use weather stations on the Antarctic Peninsula, model data, and Machine-Learning techniques to characterize these warm winds. We find they occur in every season, including winter when there is no sunlight to melt the snow surface. Föhn wind-induced melt accounts for 3.1% of the total melt on the Antarctic Peninsula and can be as high as 18% close to the mountains where the winds funnel through mountain canyons. Overall there has not been a significant increase in melt caused by föhn winds in the past 40 years, although the seasonality of the winds and associated melt are changing.

1. Introduction

Antarctic Peninsula (AP) surface melt has increased in the past half-century in response to anthropogenic increases in surface temperature (Barrand et al., 2013). Surface melt-induced firn air depletion and densification contribute to the hydrofracture process thought to have preceded the collapse of Larsen A and B ice shelves off the eastern coast of the AP in 1995 and 2002, respectively (Alley et al., 2018; Kuipers Munneke et al., 2014; McGrath et al., 2012). Ice shelves are the floating extensions of grounded glaciers and apply a buttress force that when lost, allows grounded glacier velocity to increase, and accelerates sea level rise (Rignot, 2004). Recently föhn winds have been identified as contributors to localized surface melt and hydrofracture in all seasons including polar winter at a single weather station on Larsen C ice shelf (Kuipers Munneke et al., 2018).

Föhn winds are warm and dry downslope winds that form on the lee side of mountain ranges like the AP. A. D. Elvidge and Renfrew (2016) hypothesized four mechanisms for föhn-warming: (1) Isentropic drawdown where cool moist air is blocked at low levels upwind of mountains, allowing warm dry air aloft to be brought to the surface, (2) release of latent heat from precipitation that changes the lapse rate and warms the surface, (3) mechanical mixing of the persistent cold boundary layer with warm air aloft, (4) lee-side descending air creates clear skies enhancing radiative heating. Föhn events are highly variable within and between seasons, with the ultimate effect on surface conditions dependent on the large-scale atmospheric flow and orographic forcing (A. D. Elvidge et al., 2015). The topographic configuration of the AP (orthogonal to the westerlies) makes föhn conditions possible in all seasons, especially in spring (SON) and fall (MAM), caused by the seasonal shift in the storm track (Cape et al., 2015). Föhn-induced surface melt reduces local albedo and could increase the likelihood of hydrofracture especially near the grounding line which is thought to be a vulnerable hinge-point (Lenaerts et al., 2016; Scambos et al., 2000).

A number of studies focus on the impacts of föhn wind on melt, surface mass balance, and ice shelf stability. Case studies of specific föhn events lasting days or weeks using remote sensing, in situ observations, and airborne measurements highlight their impact on the surface energy budget, mainly focusing on the Larsen C ice shelf (LCIS) (Bozkurt et al., 2018; Cape et al., 2015; A. D. Elvidge et al., 2016; Wiesenekker et al., 2018). Regional climate model studies combined with in situ observations have deepened understanding of the spatio-temporal impacts of föhn-induced melt, and reiterate its importance in ice shelf densification and evolution (Datta et al., 2019; Luckman et al., 2014; Turton et al., 2018). Site-specific research shows that föhn-induced surface melt is predominantly limited to the northern AP (King et al., 2017; Kuipers Munneke et al., 2018; Turton et al., 2018). Most recently A. D. Elvidge et al., (2020) studied the impact of föhn on the surface energy budget, clarifying previous contradictory findings, while exploring surface energy budget regimes on the Larsen C ice shelf. Föhn is well documented in summer though understudied in winter because large scale field campaigns are primarily conducted in the less harsh summer months (A. D. Elvidge et al., 2015).

Despite numerous föhn studies, questions persist regarding how föhn-induced melt affects the spatial melt pattern, especially south of the Larsen C ice shelf and west of the AP, what fraction of the total melt on the AP is caused by föhn winds, how melt varies through time, and how föhn-induced melt has evolved on the AP. To address these questions, we use a novel approach to identify föhn-induced melt events, using in situ meteorological observations to train a Machine Learning algorithm to identify the föhn signature in ERA5 global reanalysis and RACMO2 regional climate model simulations. We use these datasets to extend what we learn at weather stations both spatially and temporally. These records of föhn-induced melt occurrence, both spatial and temporally resolved are combined with the surface energy budget which allows us to quantify melt when föhn occurs. We identify a föhn-induced melt climatology, and the annual drivers of föhn variability and evolution by assessing the correlation and seasonal variability of meteorological and energy balance variables to föhn-induced melt on the AP.

2. Data and Methods

2.1. Study Domain

The AP extends 1,300 km north from the Antarctic Continent (Figure 1). The AP is covered by a grounded ice sheet and supports three major ice shelves including the fourth-largest Antarctic ice shelf (Larsen C). The spine of the AP, the Antarctic Peninsular mountain range, averages only 50 km wide, and its mean elevation is 2,800 m above the surrounding ocean. This relatively thin and high mountain range is an effective barrier to the prevailing westerlies, segmenting the peninsula into an Antarctic maritime air mass to the west, and a colder continental air mass to the east. However, when the westerlies are strong and the meteorology forces air over the AP mountain range, relatively warm and dry downslope föhn winds can increase the temperature well above the freezing point (A. D. Elvidge et al., 2015). The turbulent föhn winds disrupt the polar boundary layer which allows large fluxes of sensible heat and enhanced solar radiation to reach the surface, which are partially offset by increased latent heat exchange, causing melt (Grosvenor et al., 2014; King et al., 2017).

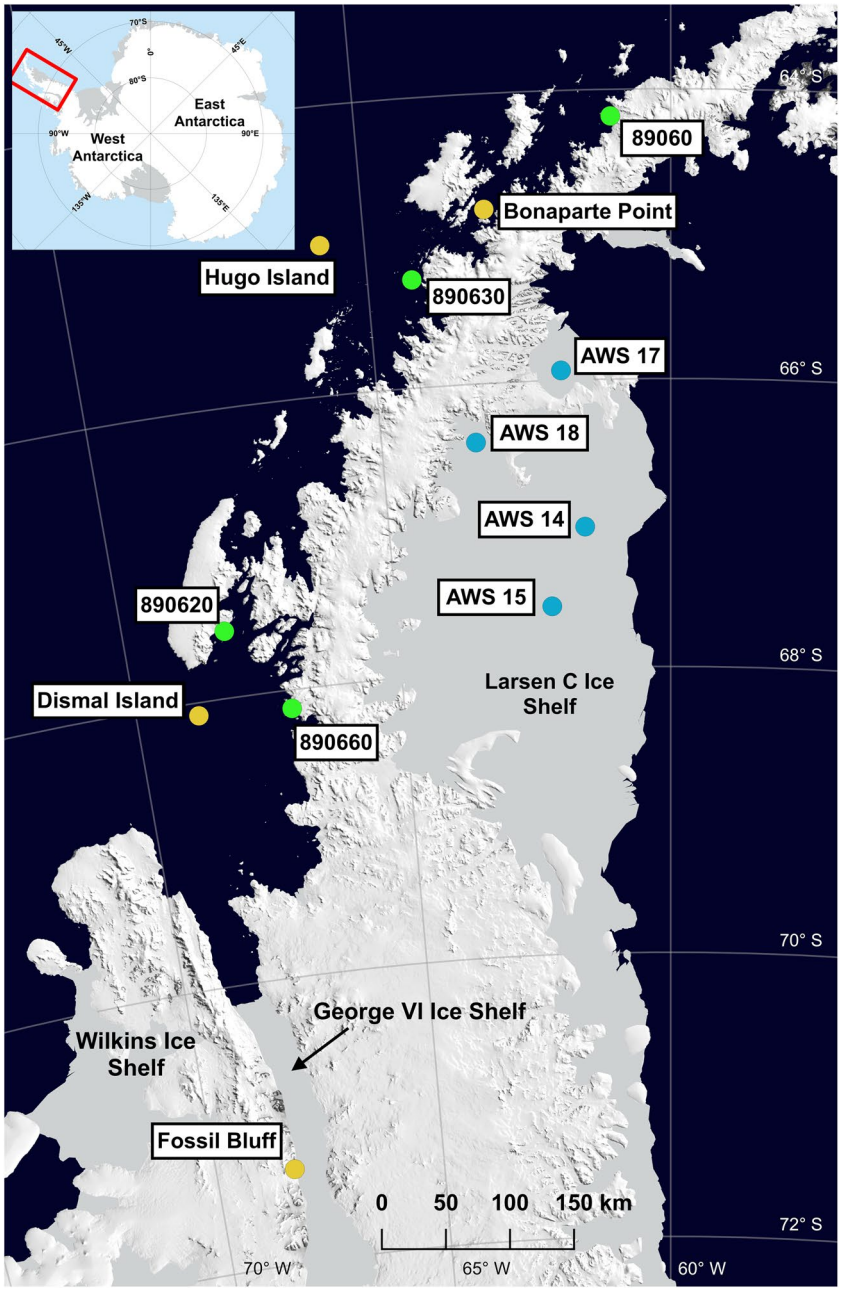

Figure 1. MODIS Mosaic overlay of the Antarctic Peninsula with automatic weather station (AWS) names and locations. Ice shelves are shaded gray and the ocean is shaded dark blue ("MODIS Mosaic of Antarctica 2008–2009 (MOA2009) Image Map, Version 1"). AWS color indicates the supporting network; Blue-Institute for Marine and Atmospheric Research (IMAU) at Utrecht University, Green-National Snow and Ice Data Center (NSIDC), Yellow-Antarctic Meteorological Research Center (AMRC) at the University of Wisconsin.

2.2. Surface Observations

We obtained in situ observations of hourly meteorological variables from three Automatic Weather Station (AWS) networks; the Institute for Marine and Atmospheric Research (IMAU) at Utrecht University, Antarctic Meteorological Research Center (AMRC) at the University of Wisconsin, Madison, and the National Snow and Ice Data Center (NSIDC). These data were processed through the Justified Automatic Weather Station (JAWS) software (Zender et al., 2019), which corrects for weather station tilt through time and harmonizes AWS data to be comparable across different networks (https://github.com/jaws/jaws).

Table 1
Automatic Weather Station Information

Station name	Location	Variables observed	Operation years
AWS 18 (IMAU)	66° 24′ S, 63° 22′ W	T, RH, W, P, WD, SW↓, SW↑, LW↓, LW↑	2015–2016
AWS 17 (IMAU)	65° 56′ S, 61° 51′ W	T, RH, W, P, WD, SW↓, SW↑, LW↓, LW↑	2011–2014
AWS 15 (IMAU)	67° 34′ S, 62° 09′ W	T, RH, W, P, WD, SW↓, SW↑, LW↓, LW↑	2009–2014
AWS 14 (IMAU)	67° 01′ S, 61° 30′ W	T, RH, W, P, WD, SW↓, SW↑, LW↓, LW↑	2009–2014
Bonaparte Point (AMRC)	64° 46′ S, 63° 03′ W	T, RH, W, P, WD	2014–2015
Dismal Island (AMRC)	68° 05′ S, 68° 49′ W	T, RH, W, P, WD	2017–2018
Fossil Bluff (AMRC)	71° 19′ S, 68° 16′ W	T, RH, W, P, WD	2009–2011
Hugo Island (AMRC)	64° 57′ S, 65° 40′ W	T, RH, W, P, WD	2009–2010
890600 (NSIDC)	64° 10′ S, 64° 10′ W	T, RH, W, P, WD	1979–1981
890620 (NSIDC)	67° 34′ S, 68° 58′ W	T, RH, W, P, WD	1988, 2001
890630 (NSIDC)	65° 15′ S, 64° 16′ W	T, RH, W, P, WD	1986–1991
890660 (NSIDC)	68° 07′ S, 67° 07′ W	T, RH, W, P, WD	1985–1997

Notes. IMAU is Institute for Marine and Atmospheric Research at Utrecht University, AMRC is Antarctic Meteorological Research Center at the University of Wisconsin, Madison, NSIDC is the National Snow and Ice Data Center. T, temperature, RH, relative humidity, W, wind speed, P, surface air pressure, WD, wind from direction, SW↓, incoming short-wave radiation, SW↑, outgoing short-wave radiation, LW↓, incoming long-wave radiation, LW↑, outgoing long-wave radiation.

Meteorological records including wind speed (m/s), air temperature (K), and relative humidity (%) were collected by 12 AWS totaling 47 station-years on the AP (Figure 1 and Table 1). AWS observations are used as ground truth, useful to evaluate satellite observations and model simulations, and are used to train a Machine Learning (ML) algorithm to detect föhn winds in reanalysis and regional climate model simulations.

2.3. Föhn Detection

We developed a Föhn Detection Algorithm (FöhnDA) that identifies föhn winds that cause melt. Our approach is similar to previous studies that employ thresholds to identify föhn conditions in hourly AWS data (Cape et al., 2015; Datta et al., 2019; A. D. Elvidge et al., 2020; Speirs et al., 2012; Turton et al., 2018), however, we are most interested in föhn-induced melt so we focus on föhns that cause the surface air temperature to rise above the freezing point. The föhn signature is quite distinct from the climatological average and is characterized by high wind speeds, low relative humidity, and increased temperatures, which makes identifying föhn events straightforward in AWS data. This signature is shared by katabatic winds, which allows FöhnDA to identify both wind types. Katabatic winds form when cold dense air drains downslope due to gravity. However, the majority of wind-induced melt in this region is the direct result of the AP spine interacting with large scale mesocyclones leading to föhn wind.

FöhnDA identifies a föhn-induced melt event using binary classification when three measured fields surpass their empirically derived thresholds. The FöhnDA threshold for air temperature (T) is 0°C, which ensures it captures föhn events that cause surface melt. Thresholds for relative humidity (RH) and wind speed (WS) are more dynamic because high wind speeds and low relative humidity do not guarantee temperatures above freezing, they only aid to identify föhn. FöhnDA uses quantile regression to identify these variable thresholds that take into account the climatology and seasonality at each weather station site. FöhnDA uses two empirically determined thresholds: the 60th percentile wind speed and 30th percentile relative humidity. Thresholds for both wind speed and relative humidity were extensively tested to help improve classification. Varying these thresholds by 10 percent above and below the current values does not produce significantly different results because the main determinant of föhn-induced melt events is a surface temperature above freezing. A föhn melt hour (h) is identified when,

$$\text{FöhnDA}(\text{h}) = 1 \;\; \text{If} \;\; \text{T} > 0°\text{C}, \;\; \text{RH} \left\langle \;\; 30\text{th} \;\; \text{percentile}, \;\; \text{WS} \right\rangle \;\; 60\text{th} \;\; \text{percentile}$$

Periods that meet these three criteria are classified as föhn melt events. We apply FöhnDA to all 12 AWS separately to produce the "ground-truth" training data for the ML algorithm to detect föhns that cause melt in reanalysis and climate model simulations. By applying FöhnDA separately at each AWS we obtain ground-truth data that encompass the climatic variability at each AWS site, and form a diverse training data set.

Finally, all AWS time series were manually quality controlled before analysis. Across all the AWS time series, FöhnDA correctly classified 97% of föhn melt events, relative to manual classification. We also conducted a föhn classification sensitivity study (Table A1) where we compare our classification results to results from methods in previous studies (Cape et al., 2015; Datta et al., 2019). Since other classification methods aim to identify all (not only melt-inducing) föhn events, we sub-sampled each method's results when temperatures were above freezing and found that FöhnDA replicated these results with less than a 5% error and with minimal false-positive and false-negative scores. We found that FöhnDA has a more sensitive wind speed criteria because the mean 60th percentile wind speed across all AWS sites is 2.85 m/s, which is exceeded during calmer föhn conditions compared to the other methods that employ higher wind speed thresholds (Datta et al, 2019–>3.5 m/s, Cape et al., 2015–>5 m/s).

2.4. Reanalysis

We used hourly meteorological data of 25 fields (Table A3) from the European Center for Medium-Range Weather Forecasts (ECMWF) ERA5 reanalysis (Copernicus Climate Change Service, 2017). These data are available at a horizontal resolution of about 30 km or 0.28° globally. ERA5 is created by assimilated satellite and in situ observations into ECMWF's Integrated Forecast System (IFS). When compared with ground-truth AWS observations on the southwestern AP and LCIS, ERA5 mean surface air temperature has a warm bias and ERA5 wind speed is underestimated though overall reproduce surface observations (Bozkurt et al., 2020; Tetzner et al., 2019).

We use sea level pressure to derive four new fields to train our ML algorithm: direction to high and low pressure, and distance to high and low pressure. These are useful to identify the preferred mesoscale flow. Two time-invariant fields, distance to steepest slope and distance to the highest elevation, serve to indicate topographic controls for föhn formation. We use an elliptical search domain with an east/west diameter of 120 km and a north/south diameter of 36 km, to determine the proximity of grid cells to local topography and slope features. This search field allows the ML algorithm to find the relationship between topographic features and föhn winds. Lastly, we create a field called ERA5 FöhnDA which uses our AWS thresholds to detect föhn conditions from ERA5 air temperature, relative humidity, and wind speed.

2.5. Atmospheric Model

We accessed the 3-hourly output of 19 fields from the Regional Atmospheric Climate Model 2 (RACMO2), version 2.3p2, with a horizontal resolution of 5.5 km (0.05°) focused on the AP. RACMO2 uses the physics package CY33r1 of the ECMWF Integrated Forecast System (IFS) (https://www.ecmwf.int/en/elibrary/9227-part-iv-physical-processes\textit{{ECMWF-IFS,} 2008}) in combination with atmospheric dynamics of the High-Resolution Limited Area Model (HIRLAM), and is evaluated extensively with surface observations located in Dronning Maud Land and the LCIS (Bozkurt et al., 2020; J. M. Van Wessem et al., 2018). When compared with AWS observations on the LCIS, surface air temperature has a slight warm bias and shortwave/longwave radiation are over/under estimated due to underestimation of clouds and moisture but overall reproduce surface observations (Bozkurt et al., 2020; King et al., 2015). RACMO2 is forced at the lateral boundaries with ERA-Interim data (Dee et al., 2011) and shows improvement in the surface energy fluxes and near-surface temperature from previous versions compared with AWS observations (J. M. Van Wessem et al., 2018). Hence RACMO2 provides self-consistent surface melt estimates independent of and intermediate in scale between ERA5 and AWS.

We created seven new fields for RACMO2 analogous to those described above for ERA5: distance to high and low pressure and direction of high and low pressure, distance to the steepest slope and highest elevation, and RACMO2 FöhnDA based on the three thresholds to identify föhn in AWS data.

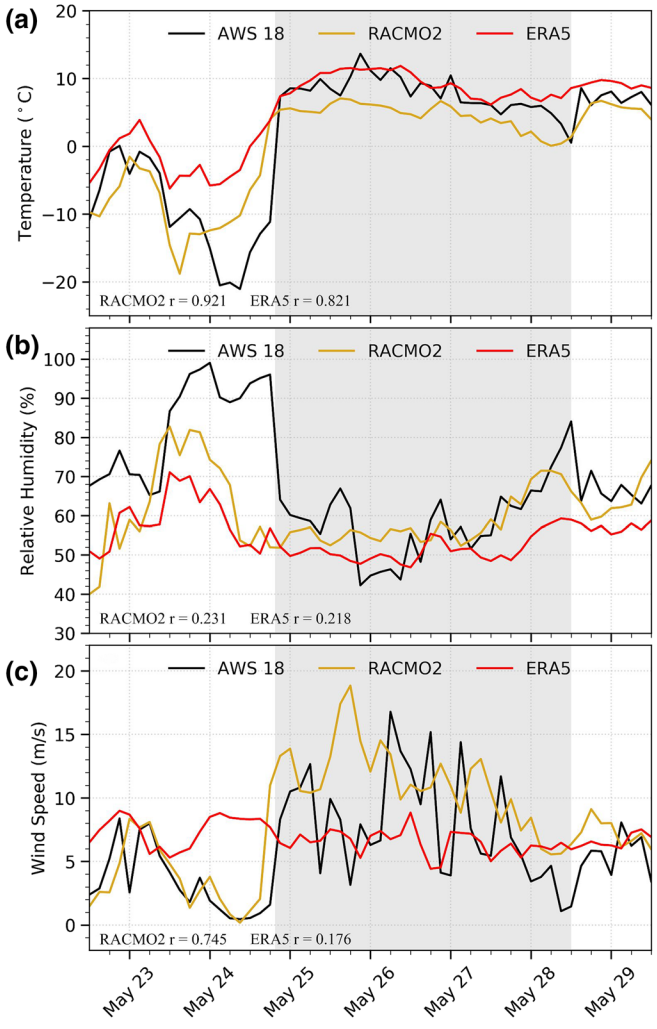

Figure 2. AWS 18 data with co-located ERA5 and RACMO2 hindcasts for a föhn wind event (shaded in gray) for (a) Air Temperature, (b) Relative Humidity, (c) Wind Speed, in late May 2016. Pearson correlation values were calculated using AWS 18 (2015–2016) with co-located ERA5 and RACMO2 for the same years. RACMO, Regional Atmospheric Climate Model.

To evaluate the consistency of ERA5 and RACMO2 meteorologies with in situ data, we intercompare their air temperature, relative humidity, and wind speed products with the nearest AWS observations. Pearson correlation values were calculated using each AWS and their operation years with co-located ERA5 and RACMO2 for the same years (Table A2). Averaged over all AWSs, Pearson r values for the spatially gridded datasets (RACMO2, ERA5) are weak for relative humidity ($r = 0.31$, $r = 0.25$) largely due to how RACMO2 and ERA5 under-represent moisture and clouds (King et al., 2015). Wind speed correlation is weak for ERA5 ($r = 0.19$) and strong with RACMO2 ($r = 0.74$), likely due to the disparity in each data set's horizontal resolution. Correlation is strong in both datasets for air temperature ($r = 0.92$, $r = 0.81$). Overall, both datasets portray spatiotemporally diffuse surface conditions relative to AWS, and thus require training to reveal the presence of localized föhn winds (Figure 2).

2.6. Machine Learning Model Development and Selection

We first attempted to detect föhn winds that cause melt in ERA5 and RACMO2 without the use of machine learning techniques by using the FöhnDA thresholds discussed above that were tuned for AWS measurements. We call this the baseline model. However, the baseline model identifies less than 50% true positives in both datasets and produces too many false-positive and false-negative föhn classifications to be useful for either gridded data set. The low accuracy of the baseline model stems from the coarser spatial footprint of the spatially gridded datasets compared to in situ observations, and from biases in ERA5 and RACMO2 mentioned above.

Machine Learning (ML) can largely circumvent the limitations imposed by spatial resolution because it learns from complex parameterized models and large datasets, such as ERA5 and RACMO2. Previous studies have compared expert human classification of föhn events to machine learning classification in the Alps with promising results (Mayr et al., 2018). We use Gradient Boosting Classification (GBC) machine learning because it provides simple and interpretable classification and performs well with atmospheric data (Jin et al., 2019; Sprenger et al., 2017). GBC uses decision trees as weak learners which are added in series. Each tree attempts to minimize the errors of the previous trees creating a strong classifier that provides scientific insight into which atmospheric input features are most important for identifying föhn winds with help from feature attribution techniques, discussed below. We used AWS FöhnDA results as ground-truth data to train two GBC decision tree models (ML-RACMO2 and ML-ERA5) to identify föhn winds that cause melt in ERA5 reanalysis and RACMO2.

For both models, we used 10-fold cross-validation to develop and validate decision trees using the XGBoost package in Python (Chen & Guestrin, 2016). XGBoost or "eXtreme Gradient Boosting" uses an ensemble of prediction models that are added iteratively to correct errors made by the previous model and improves model speed and accuracy while limiting resource costs. We also use the Python package Scikit-learn to identify model accuracy after it is run through XGBoost (https://scikit-learn.org/stable/about.html#citing-scikit-learn). In cross-validation, the model with the highest average accuracy score is considered the best model.

We co-locate AWS with the nearest model grid cell and use FöhnDA results to train a ML model for RACMO2 and a ML model ERA5. We use Bayesian hyperparameter optimization which aims to identify the value of each hyperparameter of a machine learning algorithm that returns the best performance when measured on a validation data set. The Bayesian optimization approach uses the information from past trials to

improve model performance and identify the optimum parameters quickly, instead of manually assigning values to hyperparameters or conducting a grid search. We use the BayesSearchCV class of scikit-optimize, a wrapper of Scikit-learn, where we assign a range of hyperparameter values to test and run the optimization until the model accuracy no longer improves. After this iterative improvement, the trained models were extrapolated across the AP domain of each data set to create climatologies of föhn wind-induced surface melt occurrence.

2.6.1. Model Evaluation

We evaluated the best model according to F1-score (Van Rijsbergen, 1979. The F1 score is a function of Precision and Recall, defined as,

$$\text{Precision} = \frac{\text{TruePositive}}{\text{TruePositive} + \text{FalsePositive}}$$

$$\text{Recall} = \frac{\text{TruePositive}}{\text{TruePositive} + \text{FalseNegative}}$$

$$F1 = 2 \times \frac{\text{Precision} \times \text{Recall}}{\text{Precision} + \text{Recall}}$$

Precision is defined as the number of true positives divided by the sum of true and false positives. It represents the proportion of AWS observed föhn melt events that the model predicted. Recall is defined as the number of true positives divided by the sum of true positives and false negatives. It represents the proportion of AWS-observed föhn melt events that were accurately identified by the model. The F1 statistical metric assesses model accuracy using binary classification. It takes into account both false-negative classification and false-positive classification for a range between 0 and 1. A model that correctly classifies all events with only true positive results (i.e., with no false negatives and/or false positives) yields an F1-score of 1.0. Conversely, a model that produces no true positive event classifications, and only false negative and/or false-positive results, yields an F1-score of 0.0.

A second way we evaluate model performance is to compare how well the model classification corroborates AWS-FöhnDA classified föhn events. We compared both ERA5 and RACMO2 classified föhn to 4 weather stations (AWS 14, AWS 15, AWS 17, and AWS 18) on the Larsen C ice shelf which measured the majority of AWS-identified föhn events. We divided FöhnDA-identified föhn-melt events into strong ($T > 7°C$), moderate ($3.5°C < T < 7°C$), and weak ($T < 3.5°C$) events based on air temperature at each AWS site. We compared each model classification to determine the percentage of each event type detected. We acknowledge that ERA5 and RACMO2 output bias, such as the ERA5 warm bias in the AP region, may theoretically lead to more strong and moderate events. However, by using surface observations to inform the ML model, we combat these model biases, because the ML model identifies what the föhn signature looks like in each data set. Since we classify the föhn melt events using only the AWS temperature, we can directly compare how well each ML model detects these events. This diagnostic provides insight into which events are not captured by the ML models and helps estimate how much föhn-induced melt is not captured.

Last, we learn how the ML models make a prediction based on feature weights determined by Local Interpretable Model-Agnostic Explanations (LIME), a feature attribution technique (Ribeiro et al., 2016). Since ML-learned classifiers are complex, non-linear models, it is difficult to attribute a prediction to input variables. LIME provides a way to identify the importance of input variables for any black-box classifier, by performing perturbations to the inputs, observing the effect on the output, and estimating a feature importance weight for each variable in the input (the normalized importance weights sum to 1.0). To compute an overall ranking of each feature that applies to the whole data set, we first find the feature importance for points in each of the 10 folds of the data, then aggregate the importance weights of each feature by taking their mean. LIME thus ranks the importance of input variables to provide insight into how much a model uses the given features to make a classification, and this helps the user to combat model overfitting (Table A3). More information about LIME can be found at (https://github.com/marcotcr/lime).

2.7. Surface Energy Budget and Melt

We calculate the surface energy budget as,

$$M = SW_{net} + LW_{net} + H_S + H_L \left(W\,m^{-2}\right)$$

where SW_{net} is the net of downward and upward components of shortwave radiation, LW_{net} is the net of downward and upward components of longwave radiation, and H_S and H_L are the turbulent fluxes of sensible and latent heat. Our sign convention is that energy fluxes directed toward the surface are positive, so positive net energy warms or melts the surface. When the surface temperature exceeds the freezing point, all excess energy is used to melt the surface. We disregard a ground heat flux as it is small compared to other fluxes (Kuipers Munneke et al., 2012). ERA5 and RACMO2 produce and archive all energy fluxes. We also calculate the surface energy budget for the IMAU AWS that have radiometric instruments and measure SW_{net} and LW_{net}, while H_S and H_L are calculated using the bulk aerodynamic formulas for turbulence (Kuipers Munneke et al., 2012). We compare the estimated energy budgets for AWS that provide radiation fluxes to the ERA5 and RACMO2 surface energy budget in the co-located grid cell.

3. Results

3.1. Model Accuracy and Performance

The ML models are characterized by the 12 parameters (Table A3) that produce the most accurate summary statistics (Table 2). The three most influential parameters from Table A3 are: n_estimators which is the number of decision trees used in the forest, learning_rate which sets a learning speed so the ML models do not overfit or memorize to the training data, and max_depth which sets a maximum for the number of tree splits. More information about the other XGBoost parameters used and how to tune each can be found at (https://xgboost.readthedocs.io/en/latest/index.html).

Both ML models outperform the baseline model in all three accuracy metrics (Table 2). Despite fewer features given to the ML algorithm, ML-RACMO2 outperforms ML-ERA5. Moreover, ML-RACMO2 has 33% less training data because it is provided at a 3-hourly timescale.

Table 3 provides föhn-melt classification statistics of how much of the föhn-induced in situ melt is caused by strong, moderate, and weak föhn events, and how much of that melt is captured by the ML models for each data set. Surprisingly, strong events account for about 7% of melt caused by föhn, while weak events account for about 72% of föhn-induced melt. It is important to identify which events the models capture in order to provide model diagnostics and an accurate melt climatology. Overall the ERA5-based model classifies enough föhn events to capture 90.9% of the AWS-identified föhn melt and the RACMO2-based model captures 94.4% of AWS identified föhn melt.

Both models perform particularly well for events classified by FöhnDA as strong ($T > 7°C$) and moderate ($3.5°C < T < 7°C$) (Table 3). ML-ERA5 correctly identifies all strong events measured by AWS, and 98.9% of the moderate events, while ML-RACMO2 correctly identifies all strong and 95.9% of medium events. Weak ($T < 3.5°C$) föhn events are harder to classify largely due to the more diffuse föhn-signature in the gridded models. However, ML-ERA5 classifies 87.8% of weak events and ML-RACMO2 classifies 93.5% (Table 3). Weak event classification skill is sensitive to AWS location. AWS 18 and 17, closer to the mountain slopes, have a higher weak event classification percentage (AWS 18 ~95%, AWS 17 ~92%), compared to AWS 15 (~74%) and AWS 14(~88%) which are farther downwind. Föhn winds are funneled through local topography that accelerates winds down mountain slopes then flow decelerates downstream from the mountains.

To understand the basis for the ML models classification decisions we examine the feature weights provided by LIME (Table A2). ML-ERA5's three highest weighted features are air temperature (0.174), distance to highest elevation (0.116), and 10-m wind gust (0.062). Air temperature and 10-m wind gust are logical indicators of the warm and windy föhn signature. Distance to highest elevation is also important for classification though may indicate some overfitting because the ML algorithm makes classification decisions based on one time step and does not take into account neighboring grid cells or location. ML-RACMO2's three highest weighted features (RACMO2 FöhnDA–0.183, Temperature–0.105, Relative Humidity–0.072)

Table 2
Statistics for Best Model for Each Data Set

ERA5 model prediction accuracy summary	
F1-score	79.9 ± 3.48
Recall	81.2
Precision	78.6
Improvement in F1-score over baseline model	27.4
RACMO2 model prediction accuracy summary	
F1-score	81.3 ± 3.84
Recall	84.1
Precision	78.5
Improvement in F1-score over baseline model	23.1

Notes. The error estimates for F1 score were obtained using one standard deviation of the 10-fold F1 score means. RACMO, Regional Atmospheric Climate Model. Recall is defined as the number of true positives divided by the sum of true positives and false negatives. It represents the proportion of AWS observed föhn melt events that were accurately identified by the model. Precision is defined as the number of true positives divided by the sum of true and false positives. It represents the proportion of AWS observed föhn melt events the model predicted.

include all the fields that define the föhn signature in the AWS data. Note that even though the baseline model (RACMO2 FöhnDA) does not produce high accuracy itself, it still improves the ML algorithm for classifying föhn events.

3.2. Surface Melt Pattern

Figure 3 shows the annual mean föhn-induced surface melt for ERA5 (a) and RACMO2 (b) for the period 1979–2018. Both RACMO2 and ERA5 datasets are conducive to ML use to identify the föhn signature, however, the ERA5 spatial melt pattern is inconsistent with satellite scatterometer observations of melt days and inferred melt, and misses enhanced melt in Mill, Whirlwind, and Mobiloil inlets (Bevan et al., 2018; Trusel et al., 2013). ERA5 is a global data set that lacks the resolution to properly resolve föhn winds and therefore will not be used for further analysis of föhn wind-induced melt in this study. Below we use only RACMO2 output to analyze föhn-induced melt, which resolves a surface melt pattern more consistent with surface melt satellite observations (Figure 3b). The highest föhn-induced melt (52 mm w.e. yr^{-1}) occurs east of the AP on the Larsen C and B ice shelves at the foot of the AP mountains. High localized melt is identified in Cabinet, Mill, Whirlwind, and Mobiloil inlets where föhn winds funnel through topography to form prevalent föhn jets (Elvidge et al., 2015, 2020). The inferred melt decreases eastward from the AP mountains across the LCIS as the relatively warm and dry föhn air mixes with the cold polar boundary layer which weakens the warm föhn signature. The northern portion of the LCIS experiences more melt compared to the southern portion. This is expected as the annual mean solar insolation increases equatorward. East of the AP mountains, RACMO2 indicates föhn-induced melt on the Ronne ice shelf (south of 75°S), farther south than previous research has indicated, however, melt quantity is much less than on the LCIS (Luckman et al., 2014; McGrath et al., 2012; Turton et al., 2018).

Table 3
Classification Statistics for Each Data set AWS Classification of Strong (T > 7°C), Moderate (3.5°C < T < 7°C), and Weak (T < 3.5°C) Averaged Annually Over all AWS Sites.

ERA5 föhn classification					
	Föhn occurrence		Model classified	AWS identified	
AWS classification	ERA5 (hr)	AWS (hr)	correct	föhn melt	ML melt captured
Strong	48 (7.1%)	48 (6.4%)	100.0%	7.1%	7.1%
Moderate	212 (31.3%)	214 (28.6%)	98.9%	20.5%	20.3%
Weak	425 (62%)	483 (64.8%)	87.8%	72.4%	63.5%
			Total föhn-induced melt captured		90.9%
RACMO2 föhn classification					
AWS Classification	Föhn occurrence		Model classified correct	AWS identified föhn melt	ML melt captured
	RACMO2 (hr)	AWS (hr)	–	–	–
Strong	48 (6.9%)	48 (6.4%)	100.0%	7.1%	7.1%
Moderate	205 (29.1%)	214 (28.6%)	95.9%	20.5%	19.7%
Weak	452 (64%)	483 (64.8%)	93.5%	72.4%	67.7%
			Total föhn-induced melt captured		94.5%

Notes. The "Föhn occurrence" column represents how often each AWS classified event occurs. The "Model classified correct" column represents the percentage of each AWS föhn classification the ML model classifies correctly. The "AWS identified föhn melt" column is how much AWS identified melt is caused by each AWS classified event. The "ML melt captured" column identifies how much of the melt identified by AWS is accounted for by the ML model. AWS, with automatic weather station; RACMO, Regional Atmospheric Climate Model.

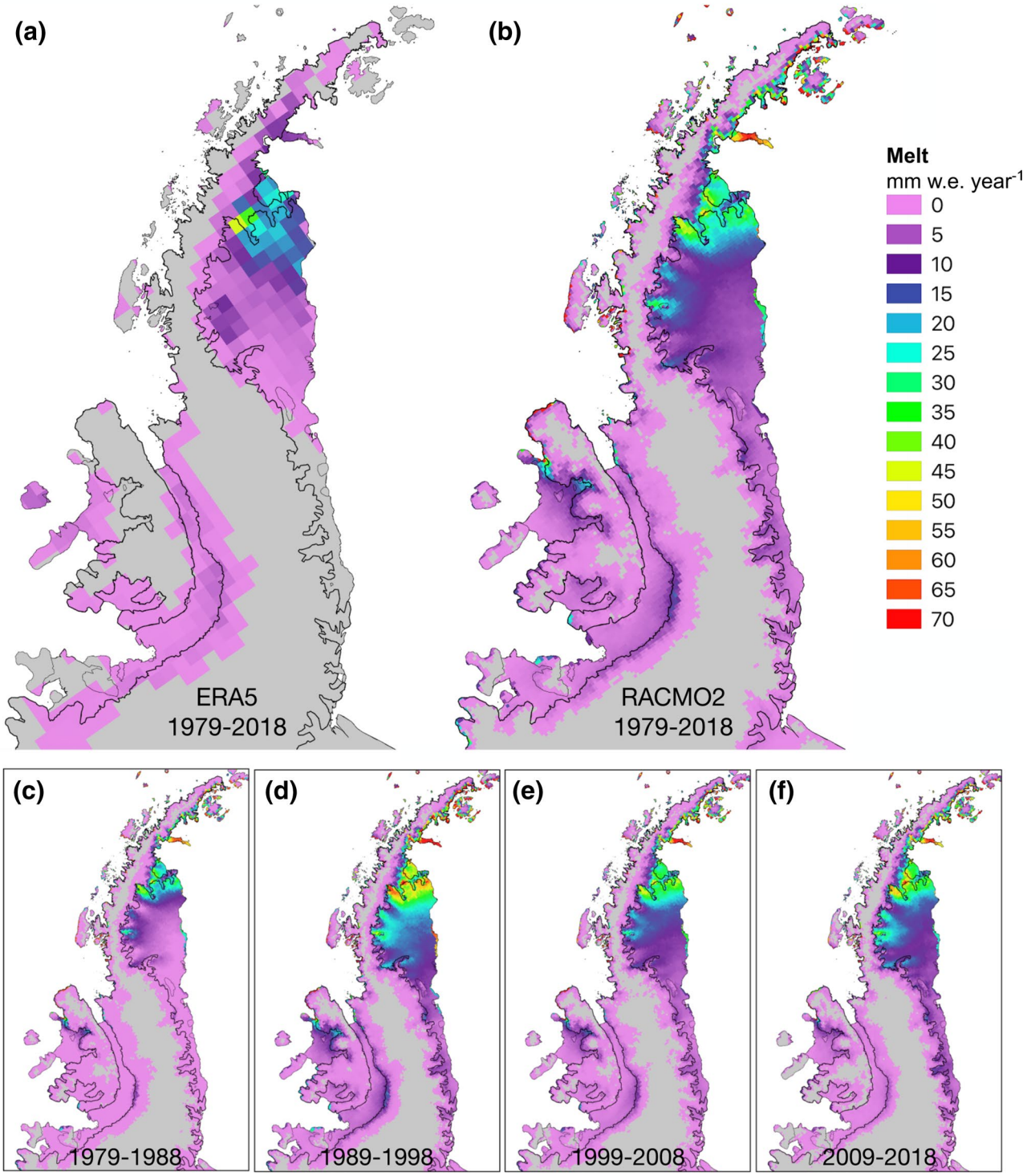

Figure 3. ERA5 (a) and RACMO2 (b) föhn-induced spatial melt patterns averaged from 1979 to 2018. RACMO2 decadal föhn-induced spatial melt pattern averaged from (c) 1979 to 1988, (d) 1989 to 1998, (e) 1999 to 2008, (f) 2009 to 2018. The thick black line indicates the grounding line from the Antarctic Surface Accumulation and Ice Discharge (ASAID) project (Bindschadler et al., 2011).

Surface melt was also inferred west of the AP on the Wilkins, Bach, and George VI ice shelves. Because föhn winds are caused by large-scale cyclonic activity it is not uncommon to have föhn winds west of the AP spine, despite the westerly prevailing wind. The primary wind direction that leads to wind-induced melt east of the AP comes from the west where air forced over the AP mountains forms föhn winds. On the Wilkins, Bach, and George VI ice shelves, the primary wind direction is also downslope though is from the northeast/east, opposite the prevailing wind direction. This could be an indicator that melt is caused by dense katabatic wind formation, especially on George VI ice shelf where the AP mountains have a long gentle slope which can inhibit föhn formation yet enhance katabatic wind formation. However, without direct observation in these regions, it is difficult to verify the mechanism behind the melt pattern.

To better explore the cause of the spatial melt pattern we examine the spatial pattern of the contribution of the positive energy balance components (sensible heat exchange and shortwave radiation) during föhn-induced melt events (Figures 4a and 4b). We find there are two melt regimes on the AP. East of the AP, surface melt during föhn events is dominated by turbulent sensible heat exchange (66%), while shortwave radiation has a more minor role (34%). This is consistent with strong föhn influence as the prevailing wind is forced over the AP spine. We also find increased sensible heat exchange in the major LCIS inlets compared to regions not impacted by strong föhn jets, previously acknowledged by A. D. Elvidge et al., 2020. West of the AP, turbulent sensible heat exchange plays an equal role with solar heating in surface melt. Sensible heat has a more central role in melt in inlets to the north and east on the Wilkins ice shelf, consistent with a northeasterly föhn influence. Farther south on the southern George VI and Bach ice shelves föhn-induced melt is driven more by clear skies and enhanced solar radiation common during föhn and less by turbulent exchange.

Overall, föhn-induced melt events occur 1.2% of the time spatially averaged over the AP, with increased occurrence East of the AP mountains (Figure 4c). Föhn-induced melt accounts for 3.1% of the total annual melt on the AP (Figure 4d). The föhn-induced melt percentage compared to the total annual melt is highest East of the AP spine at the base of the mountains, particularly in the major inlets of the LCIS. The average annual föhn-induced melt on LCIS is 3.7% of the total annual melt, however, at locations close to the AP mountains, such as at AWS 18, annual föhn-induced melt percent can reach as high as 17.7%. Even though föhn-induced melt only occurs 5.7% of the time in Cabinet inlet, that represents an average of 16.9% of the total annual melt highlighting the melting power of the föhn mechanism.

3.3. Temporal Variability and Evolution

We find the annual mean föhn-induced melt on the AP is 3.9 Gt yr^{-1} (Figure 5), about 3.1% of total annual-mean AP melt estimated by RACMO2. Annual föhn-induced melt is variable ranging from 2 Gt yr^{-1} in 1980 to 6.9 Gt yr^{-1} in 1995 (Figure 5a). Föhn-induced melt appears to increase through time (12% increase from 1979 to 2018) although the trend is not significant at the 95% level of confidence ($p = 0.48$). A significant positive trend was identified for the period 1979–1998, where föhn-induced melt increased at 0.1 Gt y^{-1}, however, this trend stabilized after 1998. These trends can be attributed to the rise in AP surface temperature from 1979 to 1998, and the decline/stabilization in AP surface temperature from 1998-present (Turner et al., 2016).

There is a clear seasonal cycle for inferred föhn-induced melt consistent with the non-föhn melt season (Figures 5b and 5c). Föhn-induced melt is highest in the summer months (DJF) when surface temperatures and shortwave radiation peak, and lowest in the winter months (JJA). Summer föhn melt constitutes 53.89% of annual föhn-induced melt on the AP. Spring and Fall surface melt contribute less (Spring (SON) 18.98%, Fall (MAM) 22.7%), while winter still experiences surface melt though much less (4.43%) than other seasons. Föhn-induced melt occurrence peaks in fall (MAM) (Figure 7a), however, the majority of föhn-induced AP surface melt occurs in summer.

Compared to the Wilkes and George VI ice shelves, LCIS contributes the most föhn-induced melt (69%) to the AP annual total, largely due to its size, low latitude, and eastern position downwind of the AP mountain range compared to other ice shelves. Wilkins and George VI ice shelves constitute much smaller portions of the total inferred AP föhn-induced melt, 3.6% and 3.7%, respectively. Föhn-induced melt has decreased with time on the Wilkes and George VI ice shelves (Figures 3c–3e, 3f). While these trends are not significant they are consistent with the larger cooling trend in the southwestern AP attributed to changes in sea ice extent and strengthening of the southern jet (Turner et al., 2016; Van; Wessem et al., 2015).

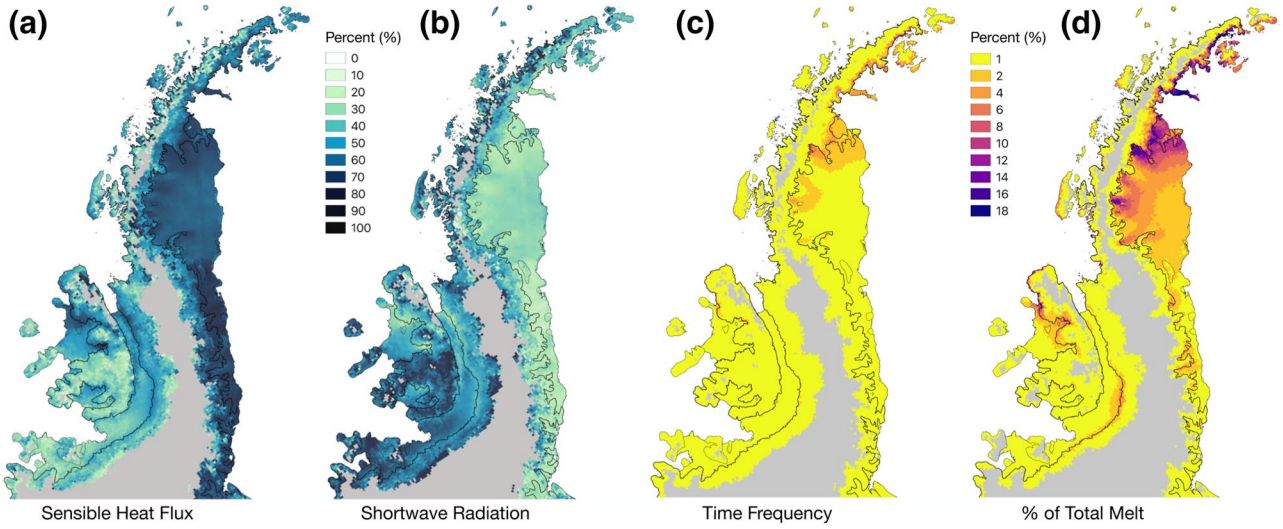

Figure 4. Map of the Sensible heat flux (a) and Shortwave radiation (b) components percent contribution of the positive energy balance during föhn-induced melt events from 1979 to 2018. (c) Map of the annual mean percent of time föhn-induced melt occurs per year from 1979 to 2018. (d) Map of the mean percent of total melt concurrent with föhn winds annually from 1979 to 2018.

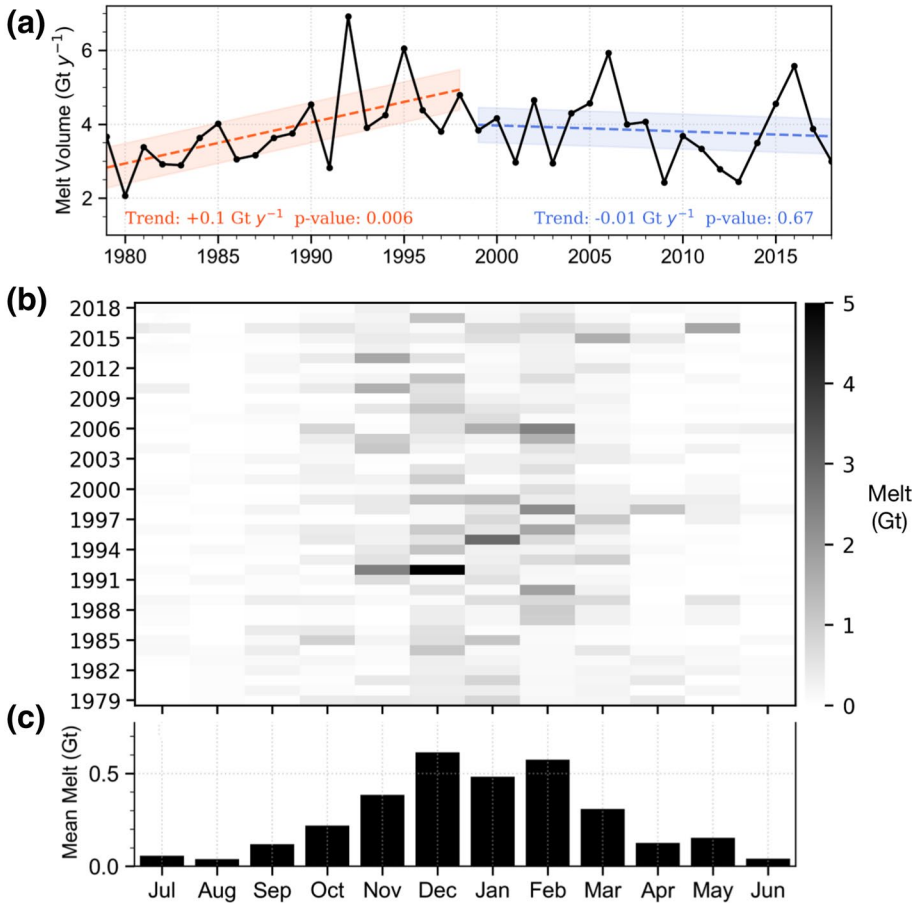

Figure 5. (a) Annual föhn-induced meltwater volume. The dashed lines indicate the linear trends for the corresponding time, with the 95% confidence limits for the trends indicated by the shaded regions. (b) RACMO2 monthly meltwater production concurrent with föhn over the AP. (c) Mean monthly (1979–2018) meltwater volume concurrent with föhn winds. AP, Antarctic Peninsula; RACMO, Regional Atmospheric Climate Model.

3.4. Föhn-Induced Melt Regime Evolution

Figure 6 shows the energy balance components, föhn occurrence, and meteorological variables related to the annual variability of föhn-induced melt events from 1979 to 2018. Each of the graphs in Figure 6 compares the föhn variable to the time series of föhn-induced surface melt, with the variable trend in color and the correlation (r) and significance level (p-value) shown. Each variable is important when trying to understand the drivers of föhn-induced melt variability through time.

Unsurprisingly, föhn-induced surface melt annual variability is most closely correlated to föhn occurrence, since föhns must be present in order to produce föhn-induced melt (Figure 6a). This is in contrast to hourly drivers of surface melt where strong sensible heat exchange and enhanced shortwave radiation drive melt, particularly in LCIS inlets (A. D. Elvidge et al., 2020). Descending föhn winds mix the stable polar boundary layer causing clear skies and increased surface temperatures. Despite this föhn mechanism driving melt, sensible heat exchange does not drive the annual variability in föhn-induced melt on the AP. Variability in the strength of the sensible heat flux has no real correlation to föhn-induced surface melt (Figure 6f). However, solar radiation, enhanced by the föhn mechanism, has a moderate correlation to föhn-induced melt, which is not unexpected because most melt in this region is driven by shortwave radiation (Figure 6b). Föhn occurrence or the number of hours föhn wind occurs AP-wide has a strong positive correlation to surface melt, implying melt variability is not driven by the strength of the föhn wind, but how much time föhn occurs (Figure 6a). This point is further illustrated by the moderate correlation of föhn-induced melt to air temperature and small air temperature variability during föhn, suggesting that föhn strength/temperature response does not change significantly through time and does not explain annual melt variability (Figure 6c).

Trends in föhn drivers indicate föhn has evolved through time. We find a long-term reduction in wind speed during föhn-induced melt events, which directly affects sensible and latent heat exchange (Figure 6d). We also see increases in shortwave radiation which are larger than the solar output variability. These trends suggest there may be sub-annual or seasonal changes through time that lead to changes in annual mean values. To better understand these seasonal changes we compared the monthly average of the first 20 years (1979–1998) to the second 20 years (1999–2018) (Figure 7). We attribute the föhn-induced melt evolution through time to a shift in seasonal föhn occurrence. We find föhn occurrence or the number of hours the AP experiences föhn-induced melt events exhibits a seasonal cycle that has changed through time. Figure 7 shows the seasonal distribution of föhn occurrence. Föhn-induced melt occurrence has a bimodal distribution and peaks during the spring and fall when the storm track shifts poleward/equatorward (Figure 7a). Figure 7b shows the monthly difference in föhn occurrence between the first 20 years (1979–1998) and the second 20 years (1999–2018). We identify large decreases in föhn occurrence in July (−34%), September (−40%), March (−13%), and April (−20%) and increased föhn occurrence in October (+21%), November (+11%), and December (+25%).

Seasonal changes in föhn-induced melt occurrence drive the change in föhn-induced melt regime on the AP. Figures 7c–7f show the seasonal variability in daily melt rate (C), wind speed (D), sensible heat exchange (E), and shortwave radiation (F) during föhn-induced melt events. Föhn-induced melt rate has a similar seasonal pattern compared to solar radiation, with a high melt rate correlated with high solar radiation. Föhn winds are strongest in the winter when vertical temperature gradients are largest due to the consistent strong polar boundary layer inversion. Since sensible heat exchange is proportional to wind speed, we see increased sensible heat exchange during winter, when föhn winds are strongest. When we compare these seasonal patterns with seasonal changes in föhn occurrence we get a clear picture of the changing AP föhn-induced melt regime. The AP experiences less föhn-induced melt events in the months when solar radiation and melt rate are low and wind speed and sensible heat exchange are high. Conversely, more melt events occur when solar radiation and melt rate is high, and when wind speed and sensible heat exchange are low. These seasonal föhn occurrence changes affect the annual mean of föhn drivers and lead to the annual trends shown in Figure 6.

4. Discussion

We extracted the föhn-induced surface melt climatology for the AP from 1979 to 2018, using a novel machine learning method to identify the föhn signature in both regional climate model simulations and in

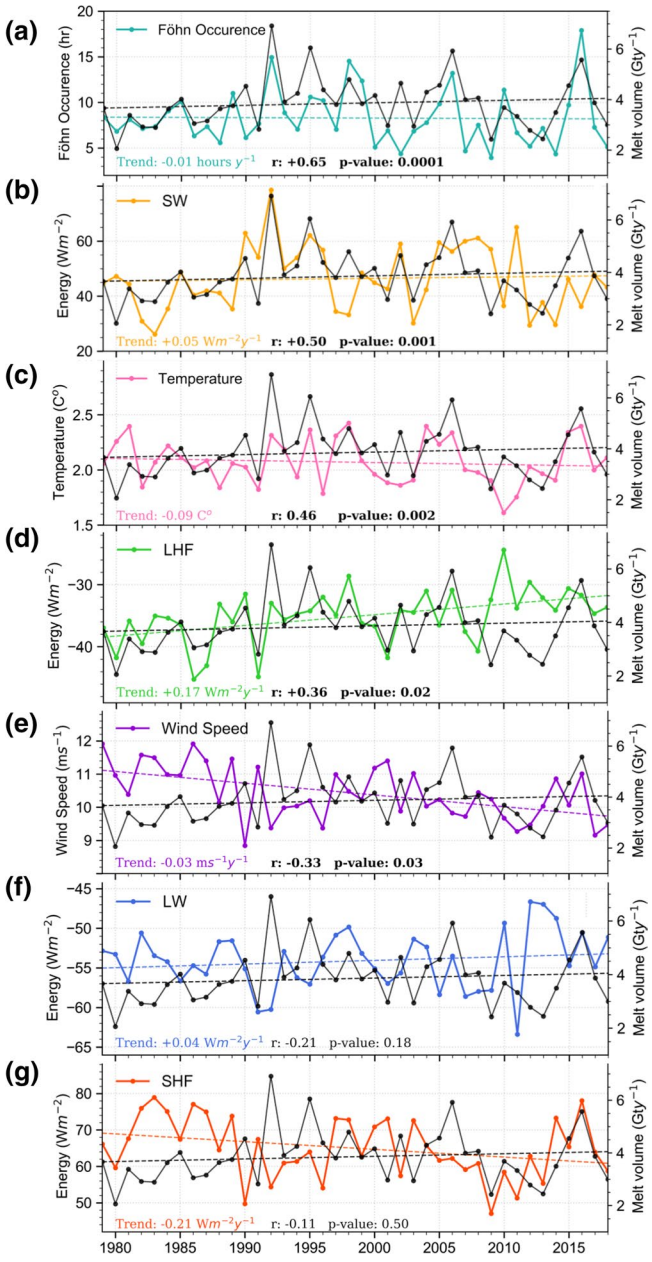

Figure 6. Time series of annual föhn-induced melt (right axis, black line) compared to: (a) föhn-induced melt occurrence, (b) shortwave radiation (SW), (c) air temperature, (d) latent heat flux (LHF), (e) wind speed, (f) longwave radiation (LW), (g) sensible heat flux (SHF). Dashed lines in each panel represent the linear trend. R values show the correlation between melt and the corresponding variable and were calculated using the Pearson correlation. P-values were considered significant at the 95% significance level (<0.05). Bold r and p-values are statistically significant.

satellite-based reanalyzes. Building on many other studies that use variable thresholds to identify föhn, we have added the additional step of using thresholds on AWS surface observations to inform a ML model what the föhn signature looks like in these datasets. Both RACMO2 and ERA5 datasets are amenable to machine learning. It is important to note that ERA5 does not resolve föhn winds, as these winds are small scale (5–20 km), especially in regions with föhn jets like Cabinet, Mill, Whirlwind, and to some extent Mobil Oil inlets (A. D. Elvidge et al., 2015). However, when we use ML informed by AWS observations, the model detects the combined changes in meteorological variables that indicate föhn presence. This means that to some extent, ERA5 represents föhn winds on the overall sense with warm, dry, and windy conditions that occur over the entire region when föhn occurs. In other words, when wind is moving from west to east, for example, over the AP mountains, the LCIS region at large will likely experience an increase in temperature, reduction in relative humidity, and increase in wind speed, which is identified by the ML algorithm, even though ERA5 does not explicitly resolve föhn events.

Our model performance was consistent with previous studies in identifying the föhn-induced melt spatial pattern and meltwater volume in RACMO2 model output (Datta et al., 2019; Kuipers Munneke et al., 2018). Although Datta et al., (2019) surface meltwater volume is slightly larger than our study (4.1 Gt yr^{-1} vs. 3.9 Gt yr^{-1}), this can be attributed to regional climate model differences, specifically grid-cell spatial resolution (Datta et al., 2019 7.5 km vs. This study at 5.5 km). Additionally, our estimates of polar night föhn induced melt agree with Kuipers Munneke et al. (2018) at AWS 18 (~23% of total melt), however, our melt volume at AWS 18 is higher (+15.2%) than RACMO2, likely due to model physics and resolution.

Our investigation into the drivers of long-term (annual) föhn-induced melt variability points to föhn-occurrence (total number of hours of föhn) and enhanced shortwave radiation as the primary drivers of melt. What is surprising is that sensible heat exchange has the weakest correlation to annual föhn-induced melt variability. This result contrasts with short-term (hourly) drivers of melt, when sensible heat is the main driver especially when shortwave radiation is limited (A. D. Elvidge et al., 2020; Kuipers Munneke et al., 2018). Locally, the influence of föhn and subsequent strength of the sensible heat exchange is primarily a function of how close a location is to the AP mountains and whether a föhn jet is present. If a location is between föhn jets or farther east on the LCIS, the sensible heat signature is less pronounced owing to a stronger shortwave radiation (cloud-clearing effect) influence (A. D. Elvidge et al., 2020). Because of this relationship, when all föhn-induced melt events are averaged annually on the AP, shortwave radiation and föhn-occurrence become the primary drivers of melt variability. Although, more research is still needed in regards to how effectively föhn winds reduce cloudiness and whether models over-represent the cloud-clearing effect and under-represent moisture during föhn (A. D. Elvidge et al., 2020; King et al., 2015).

We show that the föhn-induced melt regime has changed through time and attribute it to seasonal changes in föhn occurrence. The seasonal change in föhn occurrence may be driven by a more positive Southern Annular Mode (SAM) or Antarctic Oscillation, the defining mode of climatic variability in the AP region. A positive SAM index represents a constriction of the westerly winds toward Antarctica. Most notably the austral spring (SON) and summer (DJF) SAM index has become more positive, which shifts the storm track

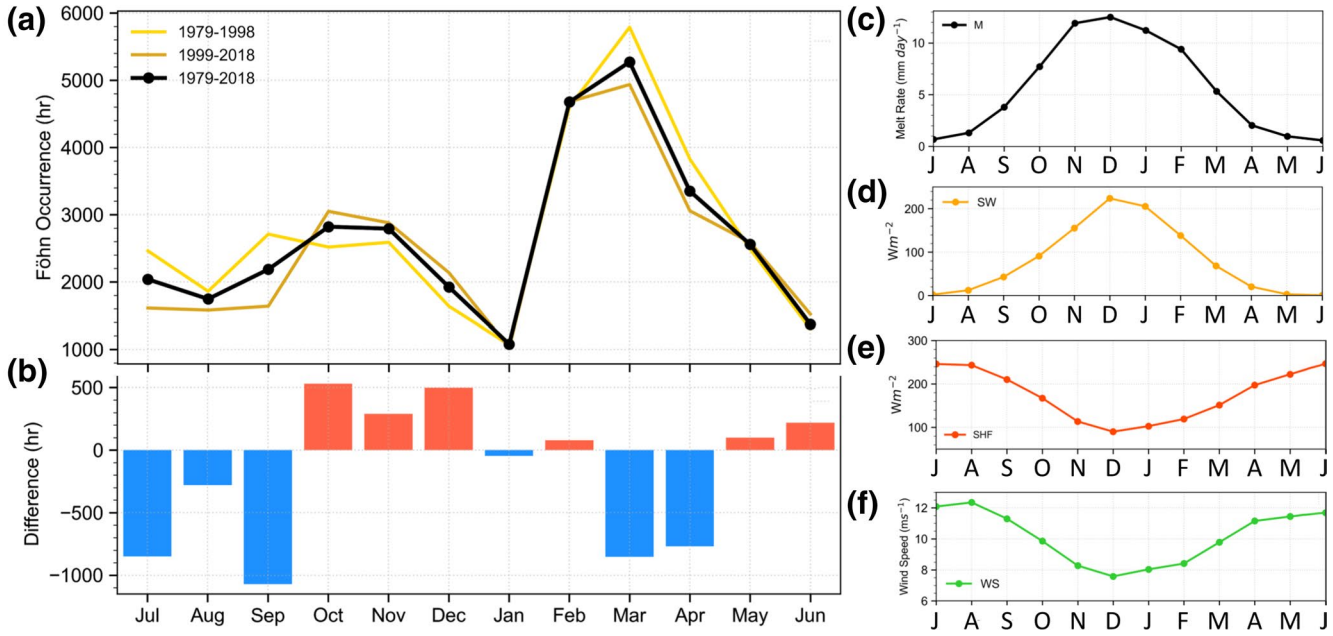

Figure 7. (a) Monthly föhn-induced melt occurrence averaged over the AP. (b) Monthly difference in föhn-induced melt occurrence between the first 20 years (1979–1998) and the last 20 years (1999–2018). (c) Monthly föhn-induced melt rate (M). (d) Monthly shortwave radiation (SW) during föhn melt events. (e) Monthly sensible heat flux (SHF) during föhn melt events. (f) Monthly average wind speed (WS) during föhn melt events. AP, Antarctic Peninsula.

southward over the AP which may cause more föhn events to occur in the region (Lubin et al., 2008). Reduced föhn occurrence in the period 1999–2018 in winter and fall is more difficult to attribute yet seems to be caused by decreased surface temperature trends identified on the AP (Turner et al., 2016). This means that there may be the same number of föhn events, though the föhn events that cause surface temperature to increase above freezing and lead to melt have decreased.

5. Conclusions

We identify föhn-induced melt events over the AP from 1979 to 2018 by using AWS surface observations to train two machine learning (ML) models to detect the föhn signature in RACMO2 and ERA5 datasets. Our ML algorithms, trained by AWS observations, performed well compared to manual classification and previous study methods. The surface melt pattern for both datasets conforms to previous work using satellite scatterometry data and model output, although ERA5 lacks the spatial resolution to resolve melt in fine-scale AP inlets such as Mill and Mobiloil. We have identified new föhn-induced melt on the Wilkes, Bach, and George VI ice shelves, consistent with eastward föhn or katabatic winds. Föhn wind-induced melt accounts for 3.1% of the total melt on the AP and can be as high at 18% close to the mountains where the winds funnel through mountain canyons to form föhn jets. Föhn-induced surface melt does not significantly increase from 1979 to 2018, despite a more positive Southern Annular Mode, however, a significant increase and subsequent decrease/stabilization occurred from 1979 to 1998 and 1999–2018, consistent with the AP warming and cooling trends during the same time periods. Föhn-induced melt occurrence and enhanced shortwave radiation drive annual variability in melt, suggesting föhn occurrence and the cloud-clearing effect of downslope wind are more important than föhn strength. We also find that the seasonality of föhn-induced melt events has evolved, driven by changes in seasonal föhn occurrence, with increased occurrence in summer, and decreased occurrence in fall, winter, and early spring. While surface temperature trends on the AP have been attributed to natural variability, changes in the SAM which affects föhn-induced surface melt occurrence, have been attributed to anthropogenic causes. This highlights the importance of further monitoring of the föhn-induced melt drivers, trends, and variability.

Journal of Geophysical Research: Atmospheres

10.1029/2020JD033682

Appendix:

Table A1
Föhn Classification Sensitivity Study Statistics

	AWS 18				AWS 17				AWS 15				AWS 14			
Study	Föhn occurrence	True positive	False positive	False negative	Föhn occurrence	True positive	False positive	False negative	Föhn occurrence	True positive	False positive	False negative	Föhn occurrence	True positive	False positive	False negative
This Study	771	771	0	0	190	190	0	0	162.5	162.5	0	0	163	163	0	0
Cape et al. 2015	742 (96.2%)	739 (95.8%)	3 (0.4%)	29 (3.8%)	193 (101.6%)	187 (98.4%)	6 (3.2%)	3 (1.6%)	159.2 (98.0%)	152.2 (93.7%)	7 (4.3%)	3.2 (2.0%)	150 (92.0%)	142 (87.1%)	8 (4.9%)	13 (8.0%)
Datta et al. 2019	757 (98.2%)	753 (97.7%)	4 (0.5%)	14 (1.8%)	180 (94.7%)	174 (91.6%)	6 (3.2%)	10 (5.3%)	160.5 (98.8%)	154.5 (95.1%)	6 (3.7%)	2 (1.2%)	159.2 (97.7%)	149 (91.4%)	10.2 (6.3%)	3.7 (2.3%)

Note: Each value is the average number of classified föhn melt event hours per year. Each of the classification methods are compared to this study. True positive represents the methods ability to correctly classify föhn hours defined by this study. False positive represents the methods classification of a föhn event when our model does not classify an event. False negative represents the method did not classify a föhn event when our model did. AWS, automatic weather station.

Table A2
Summary of Variables Used for Each Dataset

ERA5 (hourly)		RACMO2 (3-hourly)	
Variable	Feature weight	Variable	Feature weight
Time variant variables			
Temperature (K)	**0.174**	**RACMO FonDA**	**0.183**
10m wind gust (m/s)	**0.062**	**Temperature (K)**	**0.105**
ERA5 FonDA	**0.051**	**Skin Temperature (K)**	**0.073**
Month (1–12)	0.041	**Relative Humidity (%)**	**0.072**
Direction to low pressure (°)	0.038	**Sensible Heat Flux ($W \cdot m^{-2}$)**	**0.058**
Direction to high pressure (°)	0.037	Latent heat flux ($W \cdot m^{-2}$)	0.05
Snow Albedo (0–1)	0.033	Direction to high pressure (°)	0.046
Runoff (m)	0.033	Wind from direction (°)	0.043
Ice temperature (k)	0.032	Wind speed (m/s)	0.039
Wind from direction (°)	0.028	Snow evaporation (m w.e.)	0.036
Skin temperature (K)	0.027	Direction to low pressure (°)	0.031
Wind speed (m/s)	0.019	Longwave Radiation ($W \cdot m^{-2}$)	0.027
Relative humidity (%)	0.017	Snow Albedo (0–1)	0.021
Sensible heat flux ($W \cdot m^{-2}$)	0.016	Distance to low Pressure (km)	0.02
Latent heat flux ($W \cdot m^{-2}$)	0.015	Month (1–12)	0.019
Distance to low pressure (km)	0.015	Distance to high pressure (km)	0.018
Distance to high pressure (km)	0.014	Shortwave radiation ($W \cdot m^{-2}$)	0.015
Evaporation (m w.e.)	0.014	Surface pressure (hPa)	0.012
Surface pressure (hPa)	0.013	Hour of the day (0–24)	0.01
Shortwave radiation ($W \cdot m^{-2}$)	0.012	Mean sea level pressure (hPa)	0.009
Snow evaporation (m w.e.)	0.011	–	–
Longwave radiation ($W \cdot m^{-2}$)	0.011	–	–
Mean sea level pressure (hPa)	0.009	–	–
Cloud cover (0–1)	0.009	–	–
Hour of the day (0–24)	0.008	–	–
Snow depth (m w.e.)	0	–	–
Time invariant variables			
Distance to highest elevation (km)	**0.116**	Distance to highest elevation (km)	0.037
Elevation (m)	**0.049**	Latitude	0.022
Distance to steepest slope (km)	0.032	Longitude	0.021
Slope	0.029	Distance to steepest slope (km)	0.02
Longitude	0.021	Elevation (m)	0.012
Latitude	0.014	Slope	0.001

Note. Bold variables indicate the highest feature weight for each dataset.
Abbreviation: RACMO, Regional Atmospheric Climate Model.

Table A3
Machine Learning Model Summary

Data set	Algorithm	Parameter description
ERA5	Gradient boosting	n_estimators = 826, learning_rate = 0.0673, max_depth = 27, min_child_weight = 3, scale_pos_weight = 43.65, subsample = 0.65, colsample_bylevel = 0.98, colsample_bytree = 0.73, gamma = 0.06, max_delta_step = 1, reg_alpha = 0.028, reg_lambda = 6.3e-09
RACMO2	Gradient boosting	n_estimators = 995, learning_rate = 0.0263, max_depth = 50, min_child_weight = 5, scale_pos_weight = 66.66, subsample = 1.0, colsample_bylevel = 0.09, colsample_bytree = 0.44, gamma = 8.8e-09, max_delta_step = 0, reg_alpha = 1.78e-07, reg_lambda = 1e-09

Note. Each parameter is adjustable in the gradient boosting algorithm through XGBoost.
Abbreviation: RACMO, Regional Atmospheric Climate Model.

Conflict of Interest

The authors declare no conflict of interest relevant to this study.

Data Availability Statement

RACMO2 model data are available by request at https://www.projects.science.uu.nl/iceclimate/models/antarctica.php, however, a subset (2001–2018) of the data are hosted online at https://zenodo.org/record/3677642#.X-pXAFNKjUI. IMAU AWS data are available athttps://www.projects.science.uu.nl/iceclimate/aws/publications.php. Antarctic Meteorological Research Center (AMRC) AWS data are available at http://amrc.ssec.wisc.edu/aws/api/form.html. NSIDC AWS data are available at https://nsidc.org/data/nsidc-0190.

Acknowledgments
MKL was supported by the National Science Foundation (NRT-1633631) and NASA AIST (80NSSC17K0540). CSZ gratefully acknowledges support from the DOE BER ESM and SciDAC programs (DE-SC0019278, LLNL-B639667, LANL-520117). JMVW acknowledges support by PROTECT and was partly funded by the NWO (Netherlands Organisation for Scientific Research) VENI grant VI.Veni.192.083. We thank the Institute for Marine and Atmospheric Research (IMAU) at Utrecht University, the Antarctic Meteorological Research Center (AMRC) at the University of Wisconsin-Madison, and National Snow and Ice Data Center (NSIDC) for providing Automatic Weather Station data. We thank the European Center for Medium-Range Weather Forecasts (ECMWF) for providing ERA5 reanalysis data and the Institute for Marine and Atmospheric research Utrecht (IMAU) for providing RACMO2 output. We also thank the reviewers, whose suggestions greatly improved the manuscript. ERA5 reanalysis data are freely available through the European Center for Medium-Range Weather Forecasts (https://www.ecmwf.int/en/forecasts/datasets/reanalysis-datasets/era5).

References

Alley, K. E., Scambos, T. A., Miller, J. Z., Long, D. G., & MacFerrin, M. (2018). Quantifying vulnerability of Antarctic ice shelves to hydrofracture using microwave scattering properties. *Remote Sensing of Environment*, *210*, 297–306. https://doi.org/10.1016/j.rse.2018.03.025

Barrand, N. E., Vaughan, D. G., Steiner, N., Tedesco, M., Munneke, P. K., Broeke, M. R. van den, & Hosking, J. S. (2013). Trends in Antarctic Peninsula surface melting conditions from observations and regional climate modeling. *Journal of Geophysical Research: Earth Surface*, *118*(1), 315–330. https://doi.org/10.1029/2012jf002559

Bevan, S. L., Luckman, A. J., Munneke, P. K., Hubbard, B., Kulessa, B., & Ashmore, D. W. (2018). Decline in surface melt duration on Larsen C ice shelf revealed by The advanced scatterometer (ASCAT). *Earth and Space Science*, *5*(10), 578–591. https://doi.org/10.1029/2018ea000421

Bindschadler, R., Choi, H., Wichlacz, A., Bingham, R., Bohlander, J., Brunt, K., et al. (2011). Getting around Antarctica: New high-resolution mappings of the grounded and freely-floating boundaries of the Antarctic ice sheet created for the International Polar Year. *The Cryosphere*, *5*(3), 569–588. https://doi.org/10.5194/tc-5-569-2011

Bozkurt, D., Bromwich, D. H., Carrasco, J., Hines, K. M., Maureira, J. C., & Rondanelli, R., 2020: Recent near surface temperature trends in the Antarctic Peninsula from observed, reanalysis and regional climate model data. *Advances in Atmospheric Sciences*, *37*(5), 477–493. https://doi.org/10.1007/s00376-020-9183-x

Bozkurt, D., Rondanelli, R., Marín, J. C., & Garreaud, R. (2018). Foehn event triggered by an atmospheric river underlies record-setting temperature along continental Antarctica. *Journal of Geophysical Research: Atmosphere*, *123*(8), 3871–3892. https://doi.org/10.1002/2017jd027796

Cape, M. R., Vernet, M., Skvarca, P., Marinsek, S., Scambos, T., & Domack, E. (2015). Foehn winds link climate-driven warming to ice shelf evolution in Antarctica. *Journal of Geophysical Research: Atmosphere*, *120*(21), 11037–11057. https://doi.org/10.1002/2015jd023465

Chen, T., & Guestrin, C. (2016). XGBoost: A Scalable Tree Boosting System. In *Proceedings of the 22nd ACM SIGKDD International Conference on Knowledge Discovery and Data Mining–KDD 16*. ACM Press. https://doi.org/10.1145/2939672.2939785

Datta, R. T., Tedesco, M., Fettweis, X., Agosta, C., Lhermitte, S., Lenaerts, J. T. M., & Wever, N. (2019). The effect of Foehn-Induced surface melt on Firn evolution over the northeast Antarctic Peninsula. *Geophysical Research Letters*, *46*(7), 3822–3831. https://doi.org/10.1029/2018gl080845

Dee, D. P., Uppala, S. M., Simmons, A. J., Berrisford, P., Poli, P., Kobayashi, S., et al. (2011). The ERA-Interim reanalysis: Configuration and performance of the data assimilation system. *Quarterly Journal of the Royal Meteorological Society*, *137*(656), 553–597. https://doi.org/10.1002/qj.828

Elvidge, A. D., Kuipers Munneke, P., King, J. C., Renfrew, I. A., & Gilbert, E. (2020). Atmospheric drivers of melt on Larsen C Ice Shelf: Surface energy budget regimes and the impact of foehn. *Journal of Geophysical Research: Atmosphere*, *125*, e2020JD032463. https://doi.org/10.1029/2020JD032463

Elvidge, A. D., & Renfrew, I. A. (2016). The causes of Foehn warming in the Lee of mountains. *Bulletin of the American Meteorological Society*, *97*(3), 455–466. https://doi.org/10.1175/bams-d-14-00194.1

Elvidge, A. D., Renfrew, I. A., King, J. C., Orr, A., & Lachlan-Cope, T. A. (2016). Foehn warming distributions in nonlinear and linear flow regimes: Aa focus on the Antarctic Peninsula. *Quarterly Journal of the Royal Meteorological Society*, *142*(695), 618–631. https://doi.org/10.1002/qj.2489

Elvidge, A. D., Renfrew, I. A., King, J. C., Orr, A., Lachlan-Cope, T. A., Weeks, M., & Gray, S. L. (2015). Foehn jets over the Larsen C ice shelf Antarctica. *Quarterly Journal of the Royal Meteorological Society*, *141*(688), 698–713. https://doi.org/10.1002/qj.2382

Grosvenor, D. P., King, J. C., Choularton, T. W., & Lachlan-Cope, T. (2014). Downslope föhn winds over the Antarctic Peninsula and their effect on the Larsen ice shelves. *Atmospheric Chemistry and Physics*, *14*(18), 9481–9509.

Jin, Q., Fan, X., Liu, J., Xue, Z., & Jian, H. (2019). Using extreme gradient boosting to predict changes in tropical cyclone intensity over the western North Pacific. *Atmosphere*, *10*(6), 341. https://doi.org/10.3390/atmos10060341

King, J. C., Gadian, A., Kirchgaessner, A., Kuipers Munneke, P., Lachlan-Cope, T. A., Orr, A., et al. (2015). Validation of the summertime surface energy budget of Larsen C ice shelf (Antarctica) as represented in three high-resolution atmospheric models. *Journal of Geophysical Research: Atmospheres*, *120*, 1335–1347. https://doi.org/10.1002/2014JD022604

King, J. C., Kirchgaessner, A., Bevan, S., Elvidge, A. D., Munneke, P. K., Luckman, A., et al. (2017). The impact of Föhn winds on surface energy balance during the 2010–2011 melt season over Larsen C ice shelf Antarctica. *Journal of Geophysical Research: Atmosphere*, *122*(22), 12062–12076. https://doi.org/10.1002/2017jd026809

Kuipers Munneke, P. K., van den Broeke, M. R., King, J. C., Gray, T., & Reijmer, C. H. (2012). Near-surface climate and surface energy budget of Larsen C ice shelf Antarctic Peninsula. *The Cryosphere*, *6*(2), 353–363. https://doi.org/10.5194/tc-6-353-2012

Kuipers Munneke, P., Ligtenberg, S. R. M., Broeke, M. R. V. D., & Vaughan, D. G. (2014). Firn air depletion as a precursor of Antarctic ice-shelf collapse. *Journal of Glaciology*, *60*(220), 205–214. https://doi.org/10.3189/2014jog13j183

Kuipers Munneke, P. K., Luckman, A. J., Bevan, S. L., Smeets, C. J. P. P., Gilbert, E., Broeke, M. R., et al. (2018). Intense winter surface melt on an Antarctic ice shelf. *Geophysical Research Letters*, *45*(15), 7615–7623. https://doi.org/10.1029/2018gl077899

Lenaerts, J. T. M., Lhermitte, S., Drews, R., Ligtenberg, S. R. M., Berger, S., Helm, V., et al. (2016). Meltwater produced by wind albedo interaction stored in an east Antarctic ice shelf. *Nature Climate Change*, *7*(1), 58–62. https://doi.org/10.1038/nclimate3180

Lubin, D., Wittenmyer, R. A., Bromwich, D. H., & Marshall, G. J. (2008). Antarctic Peninsula mesoscale cyclone variability and climatic impacts influenced by the SAM. *Geophysical Research Letters*, *35*, 1–4.

Luckman, A., Elvidge, A., Jansen, D., Kulessa, B., Munneke, P. K., King, J., & Barrand, N. E. (2014). Surface melt and ponding on Larsen C ice shelf and the impact of föhn winds. *Antarctic Science*, *26*(6), 625–635. https://doi.org/10.1017/s0954102014000339

Mayr, G. J., Plavcan, D., Armi, L., Elvidge, A., Grisogono, B., Horvath, K., et al. (2018). The Community Foehn Classification Experiment. *Bulletin of the American Meteorological Society*, *99*(11), 2229–2235.

McGrath, D., Steffen, K., Rajaram, H., Scambos, T., Abdalati, W., & Rignot, E. (2012). Basal crevasses on the Larsen C ice shelf Antarctica: Implications for meltwater ponding and hydrofracture. *Geophysical Research Letters*, *39*(16). https://doi.org/10.1029/2012gl052413

Ribeiro, M. T., Singh, S., & Guestrin, C. (2016). Why should I trust you?. *Proceedings of the 22nd ACM SIGKDD International Conference on Knowledge Discovery and Data Mining–KDD 16*. ACM Press. https://doi.org/10.1145/2939672.2939778

Rignot, E. (2004). Accelerated ice discharge from the Antarctic Peninsula following the collapse of Larsen B ice shelf. *Geophysical Research Letters*, *31*(18). https://doi.org/10.1029/2004gl020697

Scambos, T. A., Hulbe, C., Fahnestock, M., & Bohlander, J. (2000). The link between climate warming and break-up of ice shelves in the Antarctic Peninsula. *Journal of Glaciology*, *46*(154), 516–530. https://doi.org/10.3189/172756500781833043

Speirs, J. C., McGowan, H. A., Steinhoff, D. F., & Bromwich, D. H. (2012). Regional climate variability driven by foehn winds in the McMurdo Dry Valleys Antarctica. *International Journal of Climatology*, *33*(4), 945–958 https://doi.org/10.1002/joc.3481

Sprenger, M., Schemm, S., Oechslin, R., & Jenkner, J. (2017). Nowcasting Foehn wind events using the AdaBoost machine vearning algorithm. *Weather and Forecasting*, *32*(3), 1079–1099. https://doi.org/10.1175/waf-d-16-0208.1

Tetzner, D., Thomas, E., & Allen, C. (2019). A validation of ERA5 reanalysis data in the Southern Antarctic PeninsulaEllsworth land region and its implications for ice core studies. *Geosciences*, *9*(7), 289. https://doi.org/10.3390/geosciences9070289

Trusel, L. D., Frey, K. E., Das, S. B., Munneke, P. K., & van den Broeke, M. R. (2013). Satellite-based estimates of Antarctic surface meltwater fluxes. *Geophysical Research Letters*, *40*(23), 6148–6153. https://doi.org/10.1002/2013gl058138

Turner, J., Lu, H., White, I., King, J. C., Phillips, T., Hosking, J. S., et al. (2016). Absence of 21st century warming on Antarctic Peninsula consistent with natural variability. *Nature*, *535*(7612), 411–415. https://doi.org/10.1038/nature18645

Turton, J. V., Kirchgaessner, A., Ross, A. N., & King, J. C. (2018). The spatial distribution and temporal variability of föhn winds over the Larsen C ice shelf Antarctica. *Quarterly Journal of the Royal Meteorological Society*, *144*(713), 1169–1178. https://doi.org/10.1002/qj.3284

Van Rijsbergen, C. J. (1979). *Information retrieval* (2nd ed.) Butterworth-Heinemann.

VanWessem, J. M., van den Berg, W. J., Noël, B. P. Y., van Meijgaard, E., Amory, C., Birnbaum, G., et al. (2018). Modelling the climate and surface mass balance of polar ice sheets using RACMO2 Part 2: Antarctica (19792016). *The Cryosphere*, *12*(4), 1479–1498. https://doi.org/10.5194/tc-12-1479-2018

van Wessem, J. M., Reijmer, C. H., van den Berg, W. J., van den Broeke, M. R., Cook, A. J., van Ulft, L. H., & van Meijgaard, E. (2015). Temperature and Wind Climate of the Antarctic Peninsula as Simulated by a High-Resolution Regional Atmospheric Climate Model. *Journal of Climate*, *28*(18), 7306–7326 https://doi.org/10.1175/jcli-d-15-0060.1

Wiesenekker, J., Munneke, P. K., Broeke, M. van den, & Smeets, C. (2018). A multidecadal analysis of Föhn winds over Larsen C ice shelf from a combination of observations and modeling. *The Atmosphere*, *9*(5), 172. https://doi.org/10.3390/atmos9050172

Zender, C. S., Wang, W., & Saini, A. K. (2019). *JAWS 1.0: An extensible toolkit to harmonize and analyze polar automatic weather station datasets, manuscript in preparation for geosci. Model Dev.n*. Retrieved from https://github.com/jaws/jaws